

# Soot Oxidation and Agglomeration Modeling in a Microgravity Diffusion Flame

O. A. EZEKOYE\* and Z. ZHANG

Department of Mechanical Engineering, University of Texas at Austin, Austin, TX 78712

The global evolution of a microgravity diffusion flame is detailed. Gas species evolution is computed using a reduced finite rate chemical mechanism. Soot evolution is computed using various combinations of existing soot mechanisms. Radiative transfer is coupled to the soot and gas phase chemistry processes using a  $P_1$  spherical harmonics radiation model. The soot agglomeration model was examined to note the dependence of soot growth and oxidation processes on soot surface area predictions. For limiting cases where agglomeration was excluded from the soot evolution model, soot primary particle sizes and number concentrations were calculated, and the number of primary particles per aggregate was inferred. These computations are compared with experimental results for microgravity and nonbuoyant flame conditions.

© 1997 by The Combustion Institute

## NOMENCLATURE

$a_p$	Planck mean absorption
$a, b, c, d$	exponent constants in the reaction rate expressions
$A$	preexponential constants in reaction rate expressions
$A_s$	soot surface area per unit volume
$B$	temperature-dependent constant in reaction rate expression
$c_p$	specific heat
$C_a$	agglomeration rate constant
$C_{\min}$	number of carbon atoms in the incipient carbon particle
$C_2$	Planck's second constant
$D_{im}$	diffusion coefficient of species $i$ relative to mixture
$E$	activation energy
$f$	gas phase mixture fraction
$f_v$	soot volume fraction
$G$	irradiation
$h$	total enthalpy
$h_f^\circ$	heat of formation
$k$	constant, Arrhenius reaction rate
$N_A$	Avogadro's number
$N_c$	soot particle number density
$P$	partial pressure
$q_r$	radiative heat flux
$r$	radial coordinate, reaction rates associated with soot reaction
$R$	universal gas constant, radius of combustor

$S$	source term in the conservation equation
$Sc$	Schmidt number
$t$	time
$T$	temperature
$u$	velocity
$V_i$	diffusion velocity of species $i$
$\dot{V}$	volumetric flow rate
$W$	molecular weight
$X$	mole fraction of species $i$
$Y$	mass fraction

## Greek Symbols

$\lambda$	thermal conductivity
$\beta$	agglomeration kernel
$\mu$	dynamic viscosity
$\rho$	density
$\sigma$	Stefan-Boltzmann constant
$\dot{\omega}$	reaction rate
$\zeta$	fuel-dependent radiative constant

## Subscripts

$c$	associated with soot
$cfo$	associated with soot formation
$cox$	associated with soot oxidation
$f$	forward
$F$	fuel
$g$	gas
$o$	standard state
$i$	the $j$ th species
$r$	reverse

\*Corresponding author.

COMBUSTION AND FLAME 110: 127-139 (1997)

© 1997 by The Combustion Institute

Published by Elsevier Science Inc.

0010-2180/97/\$17.00  
PII S0010-2180(97)00067-9

$s$	soot
$t$	total
th	thermophoretic
$\infty$	radiative environment conditions

## INTRODUCTION

Although it had been anticipated, and it has since been shown that soot volume fractions do not correlate with the mixture fraction, Bilger [1] discussed the possibility of soot reaction rates being specified in terms of the mixture fraction. Three families of soot formation models (Moss et al. [2], Kennedy et al. [3], and Kent et al. [4]) are based upon the basic premise outlined by Bilger. Recent attempts to specify soot mechanisms in a fuel-specific mode (as compared to studies which assumed that the parent fuel species formed soot) have been made by Lindstedt and co-workers [5–8]. In these studies, a two-equation model for soot evolution, utilizing acetylene as the soot precursor species, is developed. The model contains rate processes for nucleation, surface growth, agglomeration, and oxidation. While it is now relatively well accepted that acetylene is the soot surface growth species, there is still not a consensus that the large Polycyclic Aromatic Hydrocarbons (PAHs) thought to initiate soot nucleation are well correlated with acetylene [9]. The predictive capability of Lindstedt's model appears not to suffer considerably from this uncertainty since the surface growth reactions contribute more to increases in the soot volume fraction than nucleation reactions. Recent measurements in subatmospheric acetylene–air diffusion flames by Sunderland et al. [10] indicate that the kinetic parameters in Leung et al.'s model are larger than experimental values. While not necessary, several features of the soot evolution process have often been excluded in models of sooting flames. The temperature field is often decoupled from soot radiation, mass is not necessarily conserved in heavily sooting flames since the fuel species is sometimes not decremented to form soot, and although oxidation by molecular oxygen is included, OH oxidation is typically not included.

In recent work [11], soot oxidation processes are incorporated into the original Moss model.

In Moss et al. [11], comparisons of computational and experimental data for a Wolfhard–Parker burner indicated that the primary oxidation species is OH. The OH and other species concentrations are taken from a laminar flamelet computation, and the OH oxidation rate is specified by Fenimore and Jones [12]. The importance of predicting the soot oxidation rates within a diffusion flame cannot be overemphasized as this mechanism eventually specifies the amount of smoke produced by the flame.

Further, a fundamental property of soot aggregates produced in hydrocarbon diffusion flames is excluded from all current soot models. The soot surface area per unit volume in all current models is calculated with the assumption that the soot aggregates are spherical. Experimental results of the morphology of soot particles clearly indicate that the aggregates are best specified as mass fractals [13, 14]. By properly accounting for the mass fractal nature of the agglomerates, the surface-area-dependent rates are affected.

In this paper, several aspects of sooting flame combustion are evaluated. Major species concentrations are determined by a finite rate chemical mechanism, and soot and gas radiation processes are computed using the spherical harmonics  $P_1$  approximation. The assumptions within the model are benchmarked by modeling a microgravity spherical counterflow acetylene–air diffusion flame and comparing the results with experimental data [15]. Currently, combined sooting combustion and radiation calculations are performed with rudimentary submodels. As a result, the gas phase species and the global temperature profiles deviate from experimental results due to relatively simple submodels for gas phase chemistry, soot chemistry, and radiation. It is important to recognize the limitations of such models, and to be careful in interpreting the effects of chemistry and radiation interactions. Comparisons with experimental data in this study are first used to establish a baseline description of the flame such that further exploration of the soot chemistry assumptions can be made. It is noted for this flame simulation that OH oxidation of soot is necessary for global predictions of the soot evolution. The OH soot oxida-

tion rate parameters from Moss et al. [11] are modified and added to the soot kinetic rate parameters of Lindstedt and co-workers. Next, the validity of the particle agglomeration assumption used in sooting flame computations is examined, and the surface area per unit volume is computed. Finally, the evolution of the average soot particle diameter is discussed, and is shown to differ significantly from normal gravity experimental measurements.

### PROBLEM FORMULATION

Atreya et al. [15] experimentally investigated the flame and soot processes in a microgravity counterflow diffusion flame. In their experiments, a porous spherical burner was used to produce a low strain rate spherical diffusion flame as shown in Fig. 1. In this figure,  $Y_{F\infty}$  and  $h_{F\infty}$  represent fuel mass fraction and total enthalpy at standard condition.  $\dot{V}$  is fuel mass flow rate.  $R$  is burner radius and  $r_f$  is flame radius. In this study, the experimental system is modeled by formulating a one-dimensional, unsteady diffusion flame in spherical coordinates. The equations governing the combustion process are

mass conservation equation

$$\frac{\partial(\rho_t r^2)}{\partial t} + \frac{\partial(\rho_t u r^2)}{\partial r} = 0 \quad (1)$$

gas phase species conservation equation

$$\rho_t r^2 \left( \frac{\partial Y_i}{\partial t} + u \frac{\partial Y_i}{\partial r} \right) = \dot{\omega}_i r^2 - \frac{\partial}{\partial r} (\rho_t Y_i V_i r^2) \quad (2)$$

gas phase enthalpy (sensible) conservation equation

$$\begin{aligned} \rho_t c_p r^2 \left( \frac{\partial T}{\partial t} + u \frac{\partial T}{\partial r} \right) &= \frac{\partial}{\partial r} \left( r^2 \left( \lambda \frac{\partial T}{\partial r} - q_r \right) \right) \\ &\quad - r^2 \sum_{i=1}^K \dot{\omega}_i h_i \\ &\quad - \rho_t r^2 \sum_{i=1}^K Y_i c_{pi} V_i \frac{\partial T}{\partial r} \\ &\quad + (-S_{cfo} h_{f,F}^o + S_{cos} h_{f,co}^o) r^2 \end{aligned} \quad (3)$$

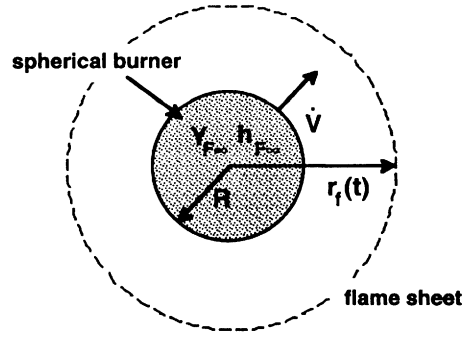


Fig. 1. Schematic diagram of spherical burner of radius  $R$  and the microgravity-maintained spherical diffusion flame of radius  $r(t)$ .

soot mass fraction conservation equation

$$\begin{aligned} r^2 \rho_t \left( \frac{\partial Y_c}{\partial t} + u \frac{\partial Y_c}{\partial r} \right) &= \frac{\partial}{\partial r} \left( r^2 \left( \frac{\mu}{Sc} \frac{\partial Y_c}{\partial r} - \rho_t u_{th} Y_c \right) \right) + r^2 S_{Y_c} \end{aligned} \quad (4)$$

soot particle number density equation

$$\begin{aligned} r^2 \rho_t \left( \frac{\partial N_c}{\partial t} + u \frac{\partial N_c}{\partial r} \right) &= \frac{\partial}{\partial r} \left( r^2 \left( \frac{\mu}{Sc} \frac{\partial N_c}{\partial r} - \rho_t u_{th} N_c \right) \right) + r^2 S_{N_c} \end{aligned} \quad (5)$$

where the total enthalpy of species  $i$  is

$$h_i = h_{fi}^o + \int_{T_o}^T c_{pi} dT. \quad (6)$$

All thermodynamic properties such as species total enthalpy, species specific heat, specific heat of gas mixture, and gas phase mixture density (which obeys the ideal gas law) are evaluated from CHEMKIN-II [16]. The transport properties such as species diffusion coefficient, thermal diffusion coefficient, thermal conductivity of mixture, and mixture dynamic viscosity are evaluated from a Gas-Phase Multicomponent Transport Properties package [17].

The fourth term on the right-hand side of the energy equation approximates the enthalpy transfer during the phase change [18]. The heat flux in the energy equation due to concentration gradients (Dufour effect) is usually small and is neglected.  $Sc$  is the Schmidt num-

ber of the soot species, and is specified to be 1000. The Schmidt number is approximately 1000 for spherical aerosol particles, with a diameter of approximately 20 nm [19]. Although the soot particles in this study are larger than 20 nm, it is found that the numerical scheme utilized (power law treatment of convective terms) introduces numerical diffusion of the same order as the Schmidt number of 1000. Thus, specifying larger values of the Schmidt number would not affect the perceived diffusion of the soot species. For both the soot mass fraction and soot particle number density equations, a thermophoretic velocity is specified by the expression of Talbot et al. [10].

### Initial and Boundary Conditions

A fuel stream exits from a spherical porous burner of radius 1.09 cm surrounded by quiescent air. The fuel mass flow rate is maintained at 22 cm<sup>3</sup>/s. The initial mixture fraction profile is assumed to be in the form of a complementary error function, with the mixture fraction specified to be unity at the burner surface and the stoichiometric value at  $r = 1.4$  cm, which is taken from the experimental results to be the initial flame location. The calculation domain is  $r = 1.09$  cm– $r = 9.09$  cm. The profiles of major species mass fraction and temperature at the initial time are interpolated as functions of mixture fraction from the experimental data of Skinner [21]. The boundary conditions at the sphere surface are

$$\frac{\dot{V}\rho_{f\infty}}{A} = \rho u \Big|_{r=R} \quad (7)$$

$$\frac{\dot{V}\rho_{f\infty}}{A} (Y_{F\infty} - Y_{FR}) = -\rho D_{Fm} \frac{\partial Y_F}{\partial r} \Big|_{r=R} \quad (8)$$

$$\begin{aligned} \frac{\dot{V}\rho_{f\infty}}{A} (h_\infty - h_R) \\ = -\lambda \frac{\partial T}{\partial r} \Big|_{r=R} + q_r \Big|_{r=R} \\ + \rho \sum_{i=1}^N h_i D_{im} \frac{\partial Y_i}{\partial r} \Big|_{r=R}. \end{aligned} \quad (9)$$

The boundary conditions at  $r = 9.09$  cm are zero flux for all dependent variables.

## CHEMICAL KINETICS MECHANISM

### Soot Kinetics

#### Mechanism Based on Molecular O<sub>2</sub> Oxidation

The soot kinetics mechanism includes soot nucleation, surface growth, oxidation, and particle coagulation steps [7]. The model has been combined with detailed chemistry simulations [5], and has been incorporated into a reduced chemical reaction mechanism [22]. The soot reaction rate terms of Fairweather et al. [7] are employed in this work as

$$k = AT^B \exp(-E/RT). \quad (10)$$

The rate constants are given in Ref. 7.

The sources in the soot mass fraction equation include the nucleation, surface growth, and O<sub>2</sub> oxidation rate terms, respectively:

$$\begin{aligned} S_{Y_c} = k_i [C_2 H_2] W_c + k_{ii} A_s [C_2 H_2] W_c \\ - k_{oi} A_s [O_2] \end{aligned} \quad (11)$$

where  $A_s$  is the soot surface area per unit volume:

$$A_s = \pi^{1/3} 6^{2/3} f_v^{2/3} (\rho N_c)^{1/3}.$$

The sources in the soot number density equation include the nucleation and agglomeration rate terms

$$\begin{aligned} S_{N_c} = \frac{2}{C_{\min}} N_A k_i [C_2 H_2] \\ - \beta \rho_i^2 W_c^{-1/6} Y_c^{-1/6} N_c^{11/6} \end{aligned} \quad (12)$$

where  $\beta = 2C_a(6W_c/\pi\rho_{c(s)})^{1/6}(6kT/\rho_{c(s)})^{1/2}$  is the agglomeration kernel. The soot kinetics constants of Fairweather are unmodified, and Fairweather specifies the number of carbon atoms in the incipient carbon particle  $C_{\min}$  to be  $9 \times 10^4$ , which results in a radius of 6 nm for incipient carbon particles.  $C_a$  is an agglomeration rate constant (3.0),  $N_A$  is Avogadro's

number ( $6.022 \times 10^{+26}$  particles  $\text{kmol}^{-1}$ ),  $k$  is the Boltzmann constant ( $1.381 \times 10^{-23}$  J  $\text{K}^{-1}$ ),  $\rho_c$  is the soot density ( $2000 \text{ kg m}^{-3}$ ), and  $W_c$  is the molar mass of carbon ( $12 \text{ kg kmol}^{-1}$ ).

It will be shown that oxidation processes are very important to accurate predictions in the microgravity flames. Consequently, the effect of the oxidation mechanism chosen was examined. Lee et al. [23] also proposed a model for soot oxidation by  $\text{O}_2$  as

$$S_{cox} = A \omega_{ox} \quad (13)$$

$$\omega_{ox} = 1.085 \cdot 10^5 X_{\text{O}_2} T^{-1/2} \exp(-E/RT) \quad (\text{kg soot/m}^2 \text{ soot/s}) \quad (14)$$

where the activation energy is 39.3 kcal/mol.

#### Additional OH Oxidation Mechanisms

The soot kinetics proposed Leung et al. [5] and Fairweather et al. [7] do not address the effects of soot consumption by the OH radical. It has been argued that in certain diffusion flame configurations, the soot oxidation path by OH can be of significant importance. A soot oxidation mechanism by the OH radical examined in this study is taken from Moss et al. [11]. The soot surface oxidation rate by OH radical is given by

$$\omega_{\text{OH}} = 1.27 \times 10^3 \Gamma X_{\text{OH}} T^{-1/2} \quad (\text{kg m}^{-2} \text{s}^{-1}) \quad (15)$$

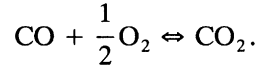
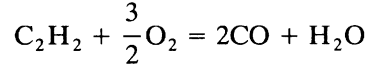
where  $\Gamma$  is a collisional efficiency and is taken to be 0.1 and  $X_{\text{OH}}$  is the OH mole fraction [11]. The soot oxidation rate by OH per unit volume is expressed by

$$S_{cos, \text{OH}} = A_s \omega_{\text{OH}} \quad (16)$$

In this study, the OH mole fraction profile in mixture fraction space is taken from the detailed chemistry calculation of Lindstedt and Mauss [24] for a low strain rate diffusion flame. The OH concentration is not included in the overall mass balance, but given the small mass fraction of OH, its effects on mass conservation are negligible. The soot OH oxidation rate term is added to the soot mass fraction equation.

#### The Gas Phase Reaction Mechanism

A two-step global reaction mechanism for the acetylene/air flame of Westbrook and Dryer [25] is employed in this study, and is given by



The reaction rate expression corresponding to the fuel decomposition reaction is

$$\dot{\omega}_1 = A \exp(-E/RT) [\text{C}_2\text{H}_2]^a [\text{O}_2]^b. \quad (17)$$

The CO oxidation reaction includes a forward and a reverse reaction which are specified by

$$\dot{\omega}_{2,f} = A \exp(-E/RT) [\text{CO}]^a [\text{H}_2\text{O}]^b [\text{O}_2]^c \quad (18)$$

$$\dot{\omega}_{2,r} = A \exp(-E/RT) [\text{CO}_2]^d. \quad (19)$$

The reaction rates due to soot formation and oxidation are included as additional source/sink term in the gas phase species conservation equations.

#### RADIATION MODEL

Under nonscattering conditions, the governing equation for the  $P1$  or differential approximation reduces to the form

$$\nabla_\tau^2 G = 3(G - 4\sigma T^4) \quad (20)$$

where  $G$  is the irradiation and  $\tau$  is the extinction coefficient. The net radiation flux is related to the irradiation by

$$\bar{q}_r = -\frac{1}{3} \bar{\nabla}_\tau G. \quad (21)$$

The boundary condition for the  $G$  is given by

$$-\frac{2 - \epsilon}{\epsilon} \frac{2}{3} \hat{n} \cdot \bar{\nabla}_\tau G + G = 4\sigma T_{bw} \quad (22)$$

where  $T_{bw}$  and  $\epsilon$  are the temperature and the emissivity at the boundary, respectively. The Planck mean absorption coefficient of the soot species can be shown to be

$$a_{p,s} = \frac{4\xi f_\nu T}{C_2} \quad (23)$$

where  $\zeta$  is a fuel-dependent constant (5),  $C_2$  is Planck's second constant,  $\sigma$  is the Stefan-Boltzmann constant [26], and  $f_v$  is the soot volume fraction. The mean absorption coefficient of the gas products  $a_{p,g}$  is taken to be a constant of  $0.0035 \text{ (cm}^{-1}\text{)}$  [27]. The total extinction coefficient is given by

$$a_p = a_{p,s} + a_{p,g}. \quad (24)$$

## SOLUTION PROCEDURE

The conservation equations are solved by a control volume finite-difference scheme. The velocity is obtained from the conservation of mass equation. All the thermodynamic properties such as specific heat of species and mixture, total enthalpy of species  $i$ , and gas phase mixture density are obtained from the CHEMKIN-II package [16]. The transport properties are calculated from the Multicomponent Transport Properties package [17]. The total density (gas phase and soot) is obtained by a local homogeneity assumption. The species mass fraction equations, soot mass fraction conservation equation, soot number density conservation equation, equation of state, and energy equation are solved iteratively at each time step. Continuity is satisfied by requiring that the summation of all species mass fractions including soot be equal to unity. To obtain a converged solution, an adaptive time-stepping routine based on the peak reaction rate magnitude is used. The criterion for the convergence of all dependent variables at each time step is a relative error less than  $10^{-3}$ . The grid was chosen for conditions where grid independence was established.

## DISCUSSIONS

### Effects of OH Oxidation (Experimental Comparisons)

Figure 2 shows the calculated flame radius (defined by the maximum flame temperature) using modified model I and experimental measurements by Atreya et al. [15]. As will be explained in more detail later, modified model I refers to calculations where the original Feni-

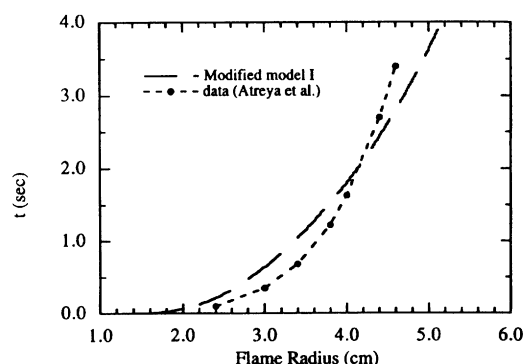


Fig. 2. Evolution of the flame radius for a  $22 \text{ cm}^3/\text{s}$  fuel flow rate, acetylene-air, microgravity diffusion flame. Comparisons are with experiments of Atreya et al.

more and Jones OH oxidation rate constant has been modified to yield better agreement with experimental data, while modified model II refers to calculations in which the agglomeration mechanism in Fairweather's model is "turned off." In Fig. 2, there is relatively good agreement between the predicted flame radius and the experimentally measured radius. Some disagreement is noted, and is attributed to computational assumptions associated with the experimental ignition procedure. In the experimental study, the flame is ignited at normal gravity (1g) conditions by hydrogen prior to the drop package being released (i.e., before  $\mu\text{g}$  conditions). In the simulations, an initial mixture fraction profile is assumed by matching the stoichiometric mixture fraction location to the initial experimentally reported flame location at the beginning of microgravity conditions. While the flame radius calculation was very insensitive to the choice of the soot model, the soot mass profile proved to be more sensitive to the model parameters.

The addition of OH oxidation to the soot evolution equations significantly modifies the flame temperature and soot mass profiles. It has been speculated that OH oxidation of soot may be larger than molecular oxygen oxidation, although not all phenomenological models incorporate this effect. In Fig. 3, predictions of the total soot mass for the spherical microgravity flame of Atreya et al. [5] are shown. Four distinct OH oxidation models are compared to the experimental data. In the first, the original model of Fairweather et al.

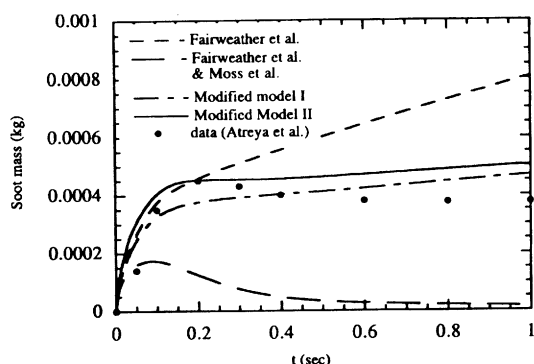


Fig. 3. Total soot mass predictions in a 22 cm<sup>3</sup>/s fuel flow rate, acetylene-air, microgravity diffusion flame. Comparisons are with experiments of Atreya et al.

[7] with no OH oxidation is shown to predict significantly larger soot mass at 1 s as compared to the experimental data. This result indicated that OH oxidation could have a significant effect on the results. In the second model, an OH oxidation rate taken from Moss et al. [11] was added to the overall soot evolution equations. The rate parameters from that model appear to overpredict the effects of OH oxidation, and the soot mass is shown to be lower than the experimental results. The Moss et al. model is an adaptation of a model presented by Fenimore and Jones [12]. Significantly better agreement with the experimental results was found by decreasing the rate term in the Moss et al. mechanism. This modification is justified given that the original Fenimore and Jones reaction rate is presented as  $\omega_{OH} = 1.63 \times 10^5 \alpha P_{O_2}^{1/4} P_{H_2O}^{1/2} T^{-1/2} e^{-37.8/RT}$  (kg m<sup>-2</sup> s<sup>-1</sup>) in contrast to Moss et al.'s modification which produces  $\omega_{OH} = 1.27 \times 10^3 \Gamma \chi_{OH} T^{-1/2}$  (kg m<sup>-2</sup> s<sup>-1</sup>). Moss et al. chose a representative temperature for the Arrhenius term and representative species concentrations to derive a rate constant (i.e.,  $1.27 \times 10^3$ ). The modified OH rate parameter which yields the best agreement with the experimental results (i.e., modified model I) is  $0.127 \times 10^3$ . A final model is shown in Fig. 3 (modified model II) which utilizes the modified OH rate (i.e.,  $0.127 \times 10^3$ ), and which also incorporates the assumption that the soot particles do not agglomerate into spherical particles. A discussion of the motivation for this modification of the soot physics is delayed until a later section, but

it should be noted that the assumption does not significantly alter the soot mass predictions. The predictive ability of soot models not utilizing OH oxidation should be questioned since, for many applications, soot oxidation processes determine the amount of smoke that is produced by the flame.

The mass-averaged soot temperature is presented in Fig. 4 for three of the four model cases presented in Fig. 3. The nonagglomerating model is not shown here. There is a far greater error in the soot average temperature when the OH mechanism taken from Moss et al. [11] is used (i.e., strongly oxidizing) as compared to the model with complete exclusion of OH oxidation [7]. For the case where the soot is strongly oxidized, the soot average temperature achieves a minimum temperature before increasing to an asymptotic value. The large soot mass case (i.e., no OH oxidation case) and the modified model I case have very nearly the same soot average temperatures. While there is more soot with the purely O<sub>2</sub> oxidizing mechanism and thus more radiative cooling, the temperature profiles are similar. The dominant heat transfer mechanism in all three flames was found to be associated with the gas radiation. There is only a slight difference among the three flame calculations presented, although there are very large differences in the amount of soot within each flame. The maximum difference in radiative heat transfer rates between the different models occurs at an early time (less than 0.5 s, and the radiative heat transfer rates differ by approximately 20% be-

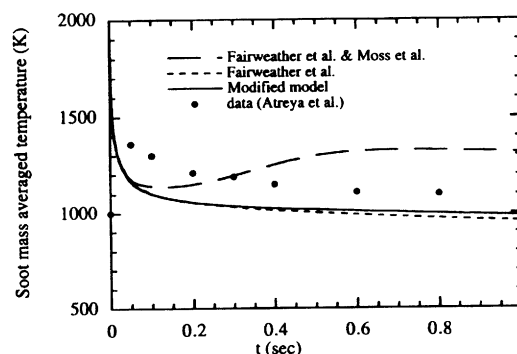


Fig. 4. Mass-averaged soot temperature is presented as a function of time for different soot chemistry model assumptions.

tween the strongly OH oxidizing flame and the solely  $O_2$  oxidizing flame. Soot radiation only modifies the radiative losses from these flames. The spherical harmonics analysis allows the soot shell to radiatively interact with the adjacent hot gas shell. This interaction tends to stabilize the soot shell temperature. The radiative loss fraction (defined as the ratio of radiant power to the chemical power associated with the fuel flow rate into the system) for this flame was calculated to be approximately 25%. This value is somewhat low for what would be expected to be a strongly radiating acetylene-air flame. By defining the radiative loss fraction as the ratio of the radiative power to the total heat release rate, a radiative loss fraction value of approximately 50% is computed (Fig. 5). It was confirmed that 50% of the fuel exiting the burner did not burn. Figure 6 shows the flame-integrated fuel consumption rate and the fuel flow rate (0.02 g/s) exiting the burner. After the ignition period, the fuel consumption rate appears to reach a quasi-steady value of approximately 0.008 g/s. The hot products and unburned gases accumulate, and very quickly radiate at a level which overshadows the soot radiative effects.

The global features of the experimentally measured temperature profiles are also predicted. These temperatures are presented in Fig. 7. The model predicts the porous burner surface temperature distribution within 8% of the experimental results. An experimentally measured temperature 2.3 cm from the burner surface is not predicted as well as the surface

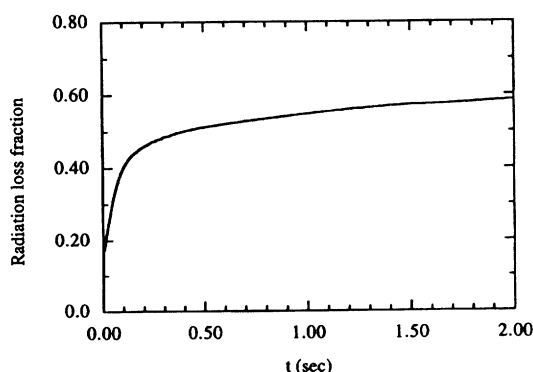


Fig. 5. Time-dependent radiative loss fraction, defined by the ratio of radiative loss rate to volume-integrated heat release rate, is presented.

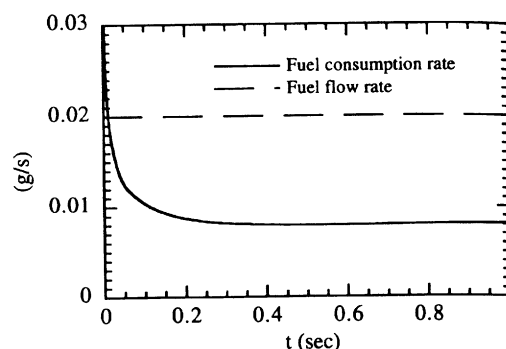


Fig. 6. Volume-integrated fuel reaction rate and fuel flow rate are shown. The ratio of the two indicates the fraction of fuel reacting within the flame.

temperature. Maximum errors of approximately 30% exist between the model and the experimental results. These errors are believed to arise both from computational assumptions and also from experimental uncertainties (which are not available). In the model development, simplifying assumptions were used which necessarily limit the predictive capabilities of the model. As in most strongly radiating flame simulations, the radiative transfer model is believed to contain the most computational uncertainties. In future studies, it will be important to assess the accuracy of the present model. The errors noted in the temperature distribution will affect the interplay of soot kinetics and gas phase kinetics. Thus, the kinetics results that are presented suggest trends more so than absolute results.

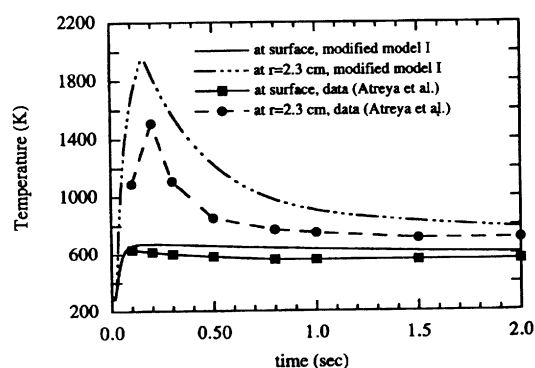


Fig. 7. Burner surface temperature and gas temperature at a radius of 2.3 cm are presented as a function of time. Comparisons are with experiments of Atreya et al.



In light of the uncertainties in the temperature calculations, qualitative statements can be made about the role of OH oxidation in this flame. The OH oxidizes relatively hot soot near the flame sheet, and does not affect cooler soot which had formed at earlier times in the flame. These effects may be seen more clearly in Figs. 8 and 9, where the soot growth rate and oxidation rates both by  $O_2$  and OH are presented per surface area of soot and per unit total volume of gas. The OH concentration used in this study is interpolated from a detailed chemistry calculation for a low-strain-rate acetylene-air diffusion flame by Lindstedt and Mauss [24]. In the present flame configuration, it is found that the soot oxidation by OH is the larger oxidation mechanism, and that oxidation by  $O_2$  is less important. The  $O_2$  oxidation mechanism of Lee et al. [23] was also used, and although the reaction rate per surface area of soot is significantly larger than the Fairweather et al. rate, it was found that all the flame predictions were insensitive to this rate change. This is not unexpected given the flame geometry. The oxidation rates by OH cover the mixture fraction space from 0.07 (stoichiometry) to approximately 0.4, beyond which the OH concentration is small. The soot formation process is on the fuel side, and extends to a mixture fraction of 0.7 (at earliest time). In contrast, the oxidation rate by  $O_2$  is strictly on the air side of the flame sheet, and very little soot crosses the flame sheet into the air side of the flame. The relative locations of the soot layer and the flame sheet in the microgravity

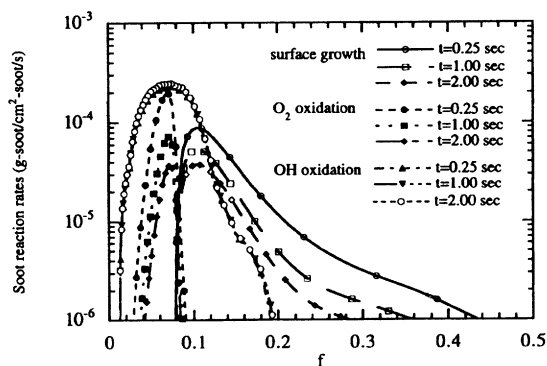


Fig. 8. Soot reaction rates (per unit area of soot) are plotted in gas phase mixture fraction space. Time after ignition is shown as a parameter.

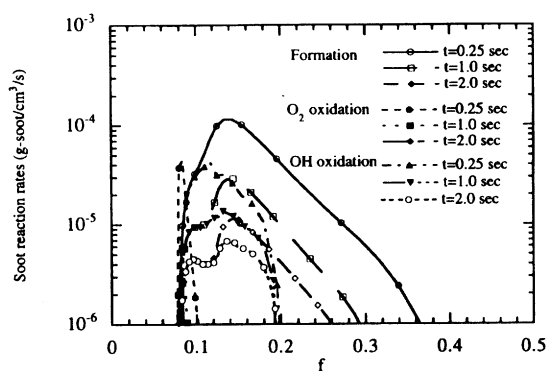


Fig. 9. Soot reaction rates (per unit volume of gas) are plotted in gas phase mixture fraction space. Time after ignition is shown as a parameter.

counterflow flame differ from observations made in normal gravity co-flow diffusion flame where the soot layer is necessarily convected into the smaller values of the mixture fraction at later times. For those conditions, soot oxidation by molecular oxygen tends to play more of a role in the complete oxidation process.

#### Effects of Coagulation Model (Soot Surface Area and Primary Particle Estimates)

Soot growth processes (surface growth and oxidation) have generally been assumed to vary linearly in the available soot surface area. An exception is the introductory study of Leung et al. [5] in which the soot surface growth rate was assumed to vary with the square root of the soot surface area in order to account for variations in the amount of reactive surface area. In later work, Fairweather et al. [11] reformulated the model such that growth processes are linear in soot surface area. In most recent studies of sooting diffusion flames, it has been assumed that the soot particles agglomerate into spherical particles. As a result, even in the absence of soot volume changes, the soot surface area decreases due to agglomeration [14, 27]. Most recent experimental studies have shown that the soot primary particles, formed in the soot nucleation step, agglomerate into cluster aggregates with identifiable primary particle components. Extensive experimental work has focused on characterizing cluster aggregates, which are also termed mass fractal agglomerates because of the scal-

ing of the aggregate mass with its characteristic length scales. It is easy to see that for these nonspherical cluster aggregate structures, the surface area per unit volume is approximated by the product of the primary particle area and the number of primary particles. Such an estimate would be exact if the primary particle spheres connected at points, but surface tension effects contribute to finite area contact joints. Thus, the total surface area per unit volume in a mass fractal agglomeration process, in the absence of nucleation, surface reaction, and oxidation reactions, should remain nearly constant. All present soot evolution models assume that soot surface area per unit volume decreases because of particle agglomeration into spherical agglomerates. The soot surface area per unit volume is shown in Fig. 10 for the baseline model (modified model I) with agglomeration assumed to occur and also without agglomeration occurring (modified model II). Due to the finite joint contact area, the actual surface area per unit volume in a flame will be between the two extremes shown in Fig. 10. The surface area per unit volume in the absence of agglomeration achieves maximum values of approximately  $50 \text{ cm}^{-1}$ , which compare favorably with the measurements of Dobbins et al. [14] where surface area per unit volume estimates are approximately  $20 \text{ cm}^{-1}$ . By not allowing the particles to agglomerate as spherical objects, the total number of primary

particles within the system increases with time. Figure 11 presents the number density in mixture fraction space at various times, and shows that in the flame region, the number densities are significantly larger for the nonagglomerating mechanism, and that on the air side of the flame, the number densities are independent of the agglomeration model. While the two sets of computational results presented in Fig. 11 evolve differently because of the area effects, the global features of the flame (e.g., soot mass variation with time) are not significantly different (Fig. 3). In an approximate sense, Fig. 11 yields information about the average number of primary particles per aggregate. The ratio of the local primary particle number density to the agglomerated number density profile yields the number of primary particles per aggregate. Examination of Fig. 11 shows that the number of primary particles per aggregate increases from order 10 near the flame sheet to a maximum value of order 10,000, and then decreases to order 1 in the fuel-rich region of the flame. It may initially appear odd that the number of primary particles within a given "aggregate" may reach 10,000, but recent soot morphology measurements by Ito et al. [28] in a microgravity diffusion flame indicate that in the absence of strong convection (i.e., cases where the soot has long residence times), the number of soot primary particles in an aggregate is significantly larger than in a normal gravity flame. Subsequent

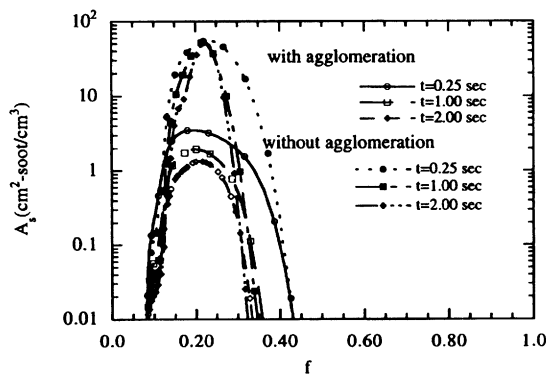


Fig. 10. Soot surface area per unit volume of gas is shown as a function of gas phase mixture fraction for two model assumptions. Particles are assumed to either agglomerate as spherical aggregates or to remain unagglomerated primary particles. Time after ignition is shown as a parameter.

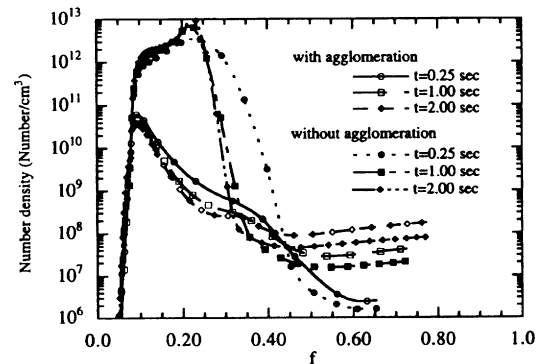


Fig. 11. Soot number density is presented as a function of gas phase mixture fraction for two model assumptions. Particles are assumed to either agglomerate as spherical aggregates or to remain unagglomerated primary particles. Time after ignition is shown as a parameter.

experiments by Ku et al. [29] support the conclusions of Ito et al. Neoh et al. [28] indicate that the OH oxidation efficiency would be modified for calculations based on fractal agglomerating processes as compared to spherically agglomerating cases. Better agreement was achieved with the experimental soot mass distribution when the soot was not assumed to aggregate and the OH rate constant was changed to  $0.203 \times 10^3$  (Fig. 12).

Using the definition of the soot particle size, it is possible to calculate the soot particle size as a function of the soot volume fraction, number density, and gas density. The soot diameter is shown in Fig. 13 for both agglomerating and nonagglomerating mechanisms. It is important to recognize that the soot kinetics model in its basic formulation predicts an incipient soot particle (6 nm) which is larger than what has been experimentally measured. For the agglomerating cases, the soot diameter is assumed to be an equivalent volume aggregate diameter. Since the total volume of an equivalent aggregate is equal to the total volume of an actual aggregate, it is possible to again estimate the number of primary particles that would be required to form the effective aggregate. These figures indicate that the relative number of primary particles within an agglomerate is consistent with the number of concentration results. The actual primary particle size computed (refer to the nonagglomerating results) is significantly larger than the initial nu-

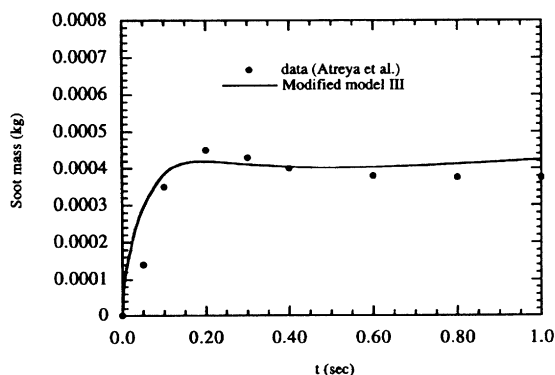


Fig. 12. Total soot mass predictions in a  $22 \text{ cm}^3/\text{s}$  fuel flow rate, acetylene-air, microgravity diffusion flame. Soot particles are assumed not to agglomerate, and OH rate constant is  $0.203 \times 10^3$ . Comparisons are with experiments of Atreya et al.

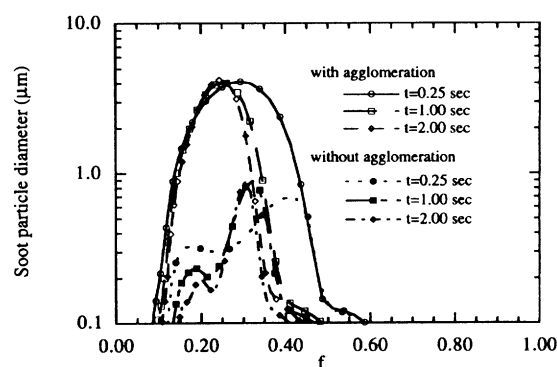


Fig. 13. Soot particle diameter is shown in mixture fraction space at different times with two different assumptions. In one case, the soot particles are assumed to agglomerate as volume equivalent spheres, and in the other case, the primary particles never agglomerate.

cleation particle size of 6 nm (computed from the assumption of a minimum number of incipient carbon particles  $C_{\min}$ ). At late times in the simulation (e.g., 1–2 s), primary particles of nearly  $1 \mu\text{m}$  diameter are computed to exist. It is unclear if these extremely large primary particle diameters are actually realized experimentally, or if these results are anomalies associated with the overall model formulation. On the other hand, it is not inconceivable that very large primary particles could grow at later times given that the computations suggest that most of the fuel flow into the flame does not actually burn. Further experiments would aid in clarifying this result. A number-averaged diameter is computed as a function of time for both the agglomerating and nonagglomerating models (Fig. 14). It is seen that at early time, the two types of calculations have the same trends. Both sets of diameters increase with respect to time until approximately 0.01 s, and subsequently decrease. The decrease is not associated with oxidation effects, but with the increase in the number of particles which have very small diameter. This is clarified by Fig. 15 which presents the growth budget for this flame, and which shows the volume-averaged contributors to the soot growth process as a function of time. For this particular flame, it is evident that only at very short times ( $t < 0.1 \text{ ms}$ ) does soot nucleation add mass to the soot mass at a larger rate than soot surface growth. Soot oxidation of OH is always larger than soot

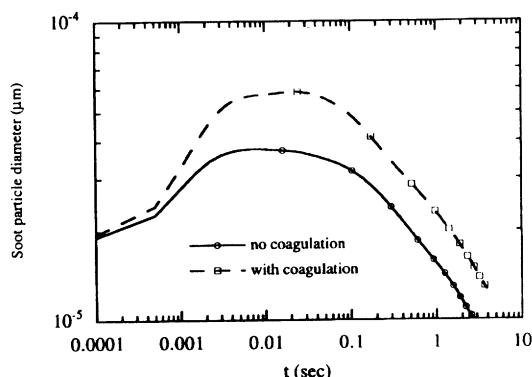


Fig. 14. Number-averaged soot diameter is presented as a function of time. Volume-equivalent diameter and primary particle results are shown.

oxidation by  $O_2$ , and at approximately 10 ms, soot oxidation begins to consume more mass than nucleation adds to the system. Finally, it is shown that only at very long times (approximately 1 s) is there a net decrease in soot mass associated with oxidation processes.

The present modeling strategy appears to be predictive of the global features of sooting diffusion flames. This is likely to be a result of rate parameters which, although individually in error, produce integrated correct trends. With increasing examination of the results of these submodels, it will be necessary to iterate upon the present model parameters to generate more predictive submodels in these systems. As an example, the effects of particle aging have not been clarified, and may necessarily alter the next level of model development. It appears that the development of an active surface area

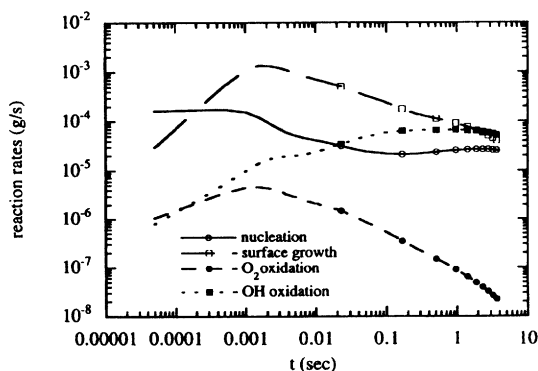


Fig. 15. Spatially integrated (total) soot reaction rates are presented as a function of time.

equation will take some time. In the meantime, it is suggested by this study that the kinetics equations for surface growth and oxidation be reformulated to better describe the actual available soot surface area.

## CONCLUSIONS

1. By using a modification of the Fairweather et al. soot model which included an OH oxidation reaction by Fenimore and Jones, the global features of a microgravity counterflow diffusion flame could be resolved. The OH oxidation reaction rate was shown to be considerably larger than the molecular oxygen reaction rate. For the counterflow flame, very little soot crosses the flame sheet into the oxygen side of the flame.

2. For microgravity diffusion flames, increased radiative heat flux measurements may be associated with the accumulated hot gas products as well as the soot radiation. For the flame configuration examined in this study, approximately 50% of the fuel does not contribute to the flame heat release.

3. The effects of soot total surface area on the global properties of the counterflow flame were examined. It is noted that for mass fractal agglomeration, the spherical agglomeration assumption significantly underpredicts the total soot surface area. The number of primary particles per aggregate and the diameter of the primary particles were estimated. It was found that the aggregate size and primary particle size were significantly larger than values measured in normal gravity flames. These increases are assumed to result from the long residence times available for continued soot growth in fuel-rich regions in the microgravity flame.

*This work is supported by the National Institute of Standards and Technology (NIST) under Grant 60NANB3D1436.*

## REFERENCES

1. Bilger, R. W., *Combust. Flame* 30:277-283 (1977).
2. Moss, B. J., Stewart, C. D., and Syed, K. J., *Twenty-Second Symposium (International) on Combustion*, The Combustion Institute, Pittsburgh, 1988, pp. 413-423.
3. Kennedy, I. M., Kollmann, W., and Chen, J. Y., *Combust. Flame* 81:73-85, 1990.

4. Kent, J. H., Jander, H., and Wagner, H. G.G., *Eighteenth Symposium (International) on Combustion*, 1981.
5. Leung, K. M., Lindstedt, R. P., and Jones, W. P., *Combust. Flame* 87:289–305 (1991).
6. Lindstedt, R. P., *IUTAM Conference on Aerothermochemistry in Combustors*, Taipei, 1991.
7. Fairweather, M., Jones, W. P., and Lindstedt, R. P., *Combust. Flame* 89 (1992).
8. Fairweather, M., Jones, W. P., Ledin, H. S., and Lindstedt, R. P., *Twenty-Fourth Symposium on Combustion*, 1992.
9. Frenklach, M., and Wang, H., in *Soot Formation in Combustion*, H. Bockhorn, Ed., Springer-Verlag, Berlin, 1994.
10. Sunderland, P. B., Koylu, U. O., and Faeth, G. M., *Combust. Flame* 100:310–322 (1995).
11. Moss, B. J., Stewart, C. D., and Young, K. J., *Combust. Flame* 101:491–500 (1995).
12. Fenimore, C. P., and Jones, G. W., *J. Phys. Chem.* 71:593–597 (1957).
13. Koylu, U. O., and Faeth, G. M., *Combust. Flame* 100:621–633 (1995).
14. Dobbins, R. A., Santoro, R. J., and Semerjian, H. G., *Twenty-Third Symposium (International) on Combustion*, Pittsburgh, 1990.
15. Atreya, A., Agrawal, S., Shamim, T., Pickett, K., Sacksteder, K. R., and Baum, H. R., NASA Microgravity Workshop, Cleveland, OH, 1995.
16. Kee, R. J., Rupley, F. M., and Miller, J. A., Sandia National Laboratories Report SAND89-8009, 1991.
17. Kee, R. J., Dixon-Lewis, G., Warnatz, J., Coltrin, M. E., and Miller, J. A., Sandia National Laboratories Report SAND86-8246, 1991.
18. Sivathanu, Y. R., and Gore, J. P., *Combust. Flame* 97 (1994).
19. Friedlander, S. K., *Smoke Dust and Haze*, Wiley, New York, 1977.
20. Talbot, L., Cheng, R. K., Schefer, R. W., and Willis, D. R., *J. Fluid Mech.* 101:737–758 (1980).
21. Skinner, S. M., Master's thesis, University of Maryland, 1990.
22. Zhang, Z., and Ezekoye, O. A., *Combust. Sci. Technol.* 112:231–255 (1996).
23. Lee, K. B., Thring, M. W., and Beer, J. M., *Combust. Flame* 6:137–145 (1962).
24. Lindstedt, R. P., and Mauss, F., *Reduced Kinetic Mechanisms for Acetylene Diffusion Flames, Lecture Notes in Physics*, N. Peters and B. Rogg, Eds., Springer-Verlag, Berlin, 1993.
25. Westbrook, C. K., and Dryer, F. L., *Combust. Sci. Technol.* 27:31–34 (1981).
26. Siegel, R., and Howell, J. R., *Thermal Radiation Heat Transfer*, Hemisphere Publishing, Singapore, 1981.
27. Saitoh, T., Yamazaki, K., and Viskanta, R., *J. Thermophys. Heat Transfer* 7(1):94–100 (1993).
28. Neoh, K. G., Howard, J. B., and Sarofim, A. F., in *Particulate Carbon: Formation During Combustion*, D. C. Siegla and G. W. Smith, Eds., Plenum, New York, 1981.
29. Ito, H., Fujita, O., and Ito, K., *Combust. Flame* 99:363–379 (1994).
30. Ku, J. C., and Roma, J., *Combust. Flame* 102:216–218 (1995).

Received 5 December 1995